ACCEPTED MANUSCRIPT

Deconvolution of Gas Diffusion Polarization in Ni/Gadolinium-Doped Ceria Fuel Electrodes

To cite this article before publication: Cedric Grosselindemann *et al* 2021 *J. Electrochem. Soc.* in press https://doi.org/10.1149/1945-7111/ac3d02

Deconvolution of Gas Diffusion Polarization in Ni/Gadolinium-Doped Ceria Fuel Electrodes

SCHOLARONE™
Manuscripts

Deconvolution of Gas Diffusion Polarization in Ni/Gadolinium-Doped Ceria Fuel Electrodes

C. Grosselindemann,[1,z] N. Russner,[1] S. Dierickx,[1] F. Wankmüller,[2] and A. Weber[1,*]

[1]Institute for Applied Materials – Electrochemical Technologies (IAM-ET), Karlsruhe Institute of Technology (KIT), Karlsruhe, D-76131, Germany,
[2]Laboratory for Electron Microscopy (LEM), Karlsruhe Institute of Technology (KIT), Karlsruhe, D-76131, Germany

*Electrochemical Society Member.

[z]E-mail: cedric.grosselindemann@kit.edu

Abstract

The deconvolution of physicochemical processes in impedance spectra of SOCs with nickel/ceria fuel electrodes is challenging as gas diffusion strongly overlaps with the electrochemical processes at fuel and air electrode. To overcome this issue, symmetrical cells were applied and the gas diffusion process at the fuel electrode was quantified by altering the inert component (nitrogen / helium) in a ternary fuel gas mixture. An effective gas transport parameter considering microstructural and geometrical features was derived, enabling a precise quantification of polarization resistances related to gas diffusion and hydrogen electrooxidation. The obtained values were applied to parameterize a dc cell model. The model validation in fuel cell and electrolyzer mode showed an excellent agreement between measured and simulated current/voltage characteristics over a wide range of technically meaningful gas compositions and operating temperatures.

Introduction

Nickel / yttria-stabilized zirconia (Ni/YSZ) fuel electrodes represent state of the art electrodes in order to reach out for high performance and durability. However, the resistance towards Ni coarsening or depletion as well as the redox stability can further be improved (1). This can be achieved by applying a nickel / gadolinium-doped ceria (Ni/CGO) cermet leading to more resilient electrodes towards carbon deposition (2), sulfur poisoning (3, 4) and redox stability (5) as well as improved electro-catalytic activity (1). The higher robustness of Ni/CGO electrodes is due to the mixed electronic/ionic conductivity of CGO (6, 7) at high temperatures and reducing atmosphere (8). In comparison to Ni/YSZ fuel electrodes, the charge transfer reactions are no longer restricted to active three phase boundaries that are necessarily in direct contact with the nickel-, the electrolyte- and the pore-matrix (8). Contact losses within the Ni-matrix are compensated by the electronic conductivity of the CGO phase. Nevertheless, there is a demand for nickel as a catalyst (9-11). In addition, a pure CGO-layer results in a drastic increase of the polarization resistance by about two orders of magnitude (12). Furthermore, a CGO layer between the Ni/CGO electrode and YSZ

electrolyte increases performance and tolerance against poisoning effects (12, 13). In contrast, the work by Nenning et al. (14) states the feasibility of a single-phase CGO fuel electrode. Yet the role of three phase boundaries at Ni/CGO electrodes compared to double phase boundaries of pure CGO electrodes towards the electrochemical performance is not clarified completely.

However, in the case of full cells exhibiting a Ni/CGO fuel electrode, an unambiguous process assignment by electrochemical impedance spectroscopy (EIS) measurements and subsequent distribution of relaxation times (DRT) analysis was not achieved up to now, since different processes in fuel and air electrodes strongly overlap in the spectrum. In a first step, symmetrical cells can be used in order to separate fuel and air electrode processes. Furthermore, the charge transfer and gas diffusion at the Ni/CGO fuel electrode also strongly overlap in the impedance spectra (3, 13,15,16). The latter is caused by the oxygen non-stoichiometry of CGO, which results in a large chemical capacity, shifting the relaxation frequency of the charge transfer process to lower relaxation frequencies (6, 15). To overcome this issue and visualize the gas diffusion process, gas mixtures containing different inert gases can be applied as shown for Ni/YSZ (17) and Ni/CGO (16, 18, 19) in previous studies.

Based on the modeling approach by Leonide et al. (20, 21) this work strives for the characterization of an electrolyte-supported solid oxide cell (ESC) with Ni/CGO fuel electrode, 3 mol-% yttria-stabilized zirconia (3YSZ) electrolyte and LSCF air electrode as well as the development of a zero-dimensional cell model for fuel cell and electrolysis mode (21, 22). Therefore, a comprehensive understanding and quantification of the individual loss processes occurring in a solid oxide cell is needed, which is also crucial regarding targeted cell development (23). In order to deconvolute the individual loss mechanisms in a solid oxide cell, EIS and the subsequent DRT analysis represent powerful methods. This approach has been successfully demonstrated for electrolyte-supported cells (ESC) (17, 24), anode-supported cells (ASC) (21) and metal supported cells (MSC) (25, 26). Applying this methodology, the physicochemical loss processes occurring in the cells can be identified by their relaxation frequencies and characteristic operating parameter dependencies. The quantification is realized by means of complex non-linear least square (CNLS)-fitting. Based on the obtained results, zero-dimensional dc cell models, which are based on common electrochemical approaches as Butler-Volmer and Fick´s laws, can be developed and parameterized.

In this study, we present a method for the deconvolution of gas diffusion and activation polarization within the Ni/CGO fuel electrode of an ESC by EIS measurements. By quantifying the associated electrochemical losses, a zero-dimensional cell model is parameterized, which is capable for predicting the cell performance over a wide technically relevant SOC operating range.

Modeling

In order to set up and parameterize a nonlinear dc performance model that considers the different loss processes in cathode, electrolyte and anode as well as further processes related to the gas transport in current collectors and gas channels a two-step approach is applied. To deconvolute and quantify the different loss processes and their operating parameter dependencies, impedance spectroscopy and impedance data analysis by the distribution of relaxation times is applied (21). Based on the peaks in the DRT and their characteristic operating parameter dependencies a linearized equivalent circuit model, representing the small signal behavior of the cell in the actual operating point, is developed and parameterized by a combined fit considering impedance and DRT data (27). From the equivalent circuit model parameters, obtained from this fit, physicochemical meaningful material and electrode parameters as exchange current densities and effective gas diffusion coefficients were deduced, enabling the simulation of the nonlinear losses in the cell at elevated current densities (21). To simulate CV characteristics of the cell an OCV minus losses model was set up (28). Starting from the open circuit voltage U_{OCV}, the cell voltage U_{cell} is calculated by subtracting ohmic losses η_{ohm}, activation losses at the fuel electrode (FE) $\eta_{\mathrm{act,FE}}$ and the air electrode (AE) $\eta_{\mathrm{act,AE}}$ as well as gas diffusion losses at the fuel $\eta_{\mathrm{diff,FE}}$ and air electrode $\eta_{\mathrm{diff,AE}}$ [1]. The equations describing the individual loss mechanisms are given in (21).

$$U_{\mathrm{cell}} = U_{\mathrm{OCV}} - \eta_{\mathrm{ohm}} - \eta_{\mathrm{act,FE}} - \eta_{\mathrm{act,AE}} - \eta_{\mathrm{diff,FE}} - \eta_{\mathrm{diff,AE}} \qquad [1]$$

Such OCV minus losses model does not only enable a performance prediction over a wide range of operating parameters but also provides quantitative information about the different voltage losses limiting the cell performance (28).

So, the ohmic law represents the proportional character of the ohmic resistance R_{ohm} towards the current density j resulting in the ohmic losses in equation [2].

$$\eta_{\mathrm{ohm}} = j \cdot R_{\mathrm{ohm}} \qquad [2]$$

In addition, the Arrhenius behavior in equation [3] is suitable for characterizing the temperature dependency of the ohmic resistance. It´s determination requires the cell specific constant B_{ohm}, the ohmic activation energy $E_{\mathrm{act,ohm}}$, the temperature T and the universal gas constant $\tilde{R}$.

$$R_{\mathrm{ohm}}(T) = \frac{T}{B_{\mathrm{ohm}}} \cdot \exp\left(\frac{E_{\mathrm{act,ohm}}}{\tilde{R}T}\right) \qquad [3]$$

Activation losses caused by the charge transfer reaction can be calculated by the Butler-Volmer approach in equation [4]. Here, $j_{0,EL}$ denotes the exchange current density, α_{EL} the charge transfer coefficient of the electrodes (EL), z the number of exchanged electrons and F the Faraday-constant.

$$j = j_{0,EL}\left[\exp\left(\alpha_{EL}\frac{zF\eta_{act,EL}}{\tilde{R}T}\right) - \exp\left(-(1-\alpha_{EL})\frac{zF\eta_{act,EL}}{\tilde{R}T}\right)\right] \qquad [4]$$

The exchange current densities for fuel $j_{0,FE}$ and air electrode $j_{0,AE}$ are shown in the equations [5] and [6] respectively. At this point, $p_{H_2,FE}$ defines the hydrogen partial pressure at the fuel electrode, $p_{H_2O,FE}$ the steam partial pressure at the fuel electrode, $p_{O_2,AE}$ the oxygen partial pressure at the air electrode and p_{ref} the reference pressure ($p_{ref} = 1$ atm). The influence of the overall pressure can be neglected since all experiments are operated under atmospheric conditions in this work. Also, a, b, and m denote the dimensionless exponents as well as γ_{EL} an exponential prefactor and $E_{act,EL}$ the activation energy of the corresponding electrode.

$$j_{0,FE} = \gamma_{FE}\left(\frac{p_{H_2,FE}}{p_{ref}}\right)^a \left(\frac{p_{H_2O,FE}}{p_{ref}}\right)^b \exp\left(-\frac{E_{act,FE}}{\tilde{R}T}\right) \qquad [5]$$

$$j_{0,AE} = \gamma_{AE}\left(\frac{p_{O_2,AE}}{p_{ref}}\right)^m \exp\left(-\frac{E_{act,AE}}{\tilde{R}T}\right) \qquad [6]$$

Gas diffusion losses $\eta_{diff,EL}$ can be described based on the Nernst-Equation and Fick´s law of diffusion in the equations [7] and [8] (29,30). Here L_{EL} denotes the thickness of the gas diffusion layer, Ψ_{EL} the microstructure parameter at each electrode side and D_i the gas diffusion coefficient of the species i, p the overall pressure and P_{corr} a conversion factor of 101330 Pa atm^{-1}.

$$\eta_{diff,FE} = \frac{\tilde{R}T}{2F}\ln\left(\frac{1 + \frac{\tilde{R}TL_{FE}}{2F\Psi_{FE}D_{H_2O}p_{H_2O,FE}P_{corr}}\cdot j}{1 - \frac{\tilde{R}TL_{FE}}{2F\Psi_{FE}D_{H_2}p_{H_2,FE}P_{corr}}\cdot j}\right) \qquad [7]$$

$$\eta_{diff,AE} = \frac{\tilde{R}T}{4F}\ln\left(\frac{1}{1 - \frac{\tilde{R}TL_{AE}\left(1 - p_{O_2,AE}/p\right)}{4F\Psi_{AE}D_{O_2}p_{O_2,AE}P_{corr}}\cdot j}\right) \qquad [8]$$

Whereas the abovementioned equations and parameter dependencies were sufficient to simulate CV-characteristics of cells exhibiting a Ni/YSZ-anode, in case of ceria additional dependencies such as the impact of the gas composition on the ohmic resistance of the cell might become essential. The required modifications of the dc performance model are discussed in the results.

Experimental

In this work planar electrolyte-supported cells with an active cell area of 1 cm^2 were investigated. The cells exhibited a Ni/CGO fuel electrode, a 3 mol-% YSZ (3YSZ) electrolyte substrate and an LSCF air electrode. Additional CGO layers were placed in between electrodes and electrolyte. The layer thicknesses were analyzed by scanning electron microscopy (SEM) yielding in a thickness for the fuel electrode of approx. 24 µm, for the electrolyte of approx. 85 µm and for the air electrode of approx. 30 µm. A schematic sketch of an experimental full cell is shown in figure 1. Furthermore, an SEM image of a focused ion beam (FIB) polished fuel electrode cross section is presented in figure 2. The FIB-polishing and SEM-imaging was performed in a SEM/FIB Thermo Scientific^{TM} Helios G4FX DualBeam^{TM} (Thermo Fisher Scientific, Waltham, Massachusetts, USA) instrument. Further information about the equipment can be found in (31). Three different cell layers become visible at this SEM image, namely the 3YSZ electrolyte 1 (cf. figure 2), a CGO interlayer 2 and a Ni/CGO fuel electrode 3. In the latter, Ni depicts the darker grey particles and CGO the lighter grey ones with black pores in between. It is visible that the Ni particle size and amount varies from bottom to top of the electrode. This further demands the investigation of the role of three phase boundaries at Ni/CGO electrodes compared to double phase boundaries of pure CGO electrodes regarding the electrochemical performance. However, a three-dimensional reconstruction of the Ni/CGO fuel electrode of this cell with a focused ion beam scanning electron microscope was not performed until now, as an adapted reconstruction procedure has to be developed first. The results will be published in another paper. In order to study the processes at cathode and anode individually, symmetrical cells with nominally identical electrodes were applied.

Testing of full and symmetrical cells was performed in a test bench described in (27). The fuel is supplied by a gas mixing unit via mass flow controllers providing gas mixtures of hydrogen H_2, oxygen O_2 as well as the inert gases nitrogen N_2 and helium He, respectively. A total flow rate of 250 sccm is set at each electrode side. Steam is produced in an upstream combustion chamber by mixing oxygen to the fuel. This enables a stable fuel humidification of up to 100 % H_2O.

After mounting the cell in the test rig, a predefined startup procedure was performed. In the following testing phase, impedance spectra and CV-characteristics were measured at systematically varied operating conditions. The spectra were acquired by a Solartron 1260 frequency response analyzer using a pseudo-potentiostatic mode (amplitude ≤ 12 mV regarding the polarization resistance (27)). The frequency was varied in between 30 mHz and 1 MHz with 12 points per decade. All experiments were conducted under open circuit conditions (OCV), except for the determination of the charge transfer coefficients α. In total about 500 impedance spectra were measured in a wide range of gas compositions in a temperature range from 600 °C to 900 °C.

The validity of the measured spectra was verified by a Kramers Kronig Test (32). Moreover, after each variation a reference measurement was conducted. The deviation between these spectra was less than 2 % proving that ageing effects can be neglected throughout all measurements.

Results and Discussion

Regarding a first analysis of processes at the cathode and the anode, impedance spectra of a full cell shall be compared with those of the electrodes taken from symmetrical cell measurements (figure 3). Figure 3 (a) shows the spectrum of the full cell, (b) of the LSCF air electrode and (c) of the Ni/CGO fuel electrode. It should be noted that in (b) and (c) the spectrum of a single electrode is displayed, i.e. the measured spectrum of the symmetrical cell divided by two, whereas in the further figures the full spectra and the related DRTs of the symmetrical cells are displayed. The different ohmic resistances can be explained by different electrolyte thicknesses of the cells. The visible deviation between the full cell and the addition of fuel and air electrode impedance taken from symmetrical cell measurements might originate from minor leakages in the full cell measurement that can be excluded in symmetrical cell measurements as well as minor temperature differences.

A more detailed analysis of the LSCF air electrode is shown in the appendix of this contribution as similar properties and parameter dependencies as reported in (21) were observed. Recapitulatory, for low oxygen partial pressures a peak at frequencies between $0.3 - 10$ Hz becomes visible in the DRT. It strongly depends on the oxidant composition but shows approximately no operating temperature dependency, and thus is attributed to the gas diffusion process in the air electrode. It should be noted that the related resistance is negligibly small for technically meaningful operating conditions. In addition, a coupling of the charge transfer with the solid-state diffusion of oxygen ions could be identified in a process around $2 - 500$ Hz, which corresponds to the oxygen reduction in the mixed electronic-ionic conducting LSCF-cathode modelled by a Gerischer element (33).

This paper focuses on results obtained from symmetrical cells with Ni/CGO electrode in order to identify and quantify the processes in the fuel electrode. The challenge to overcome in this contribution shall be illustrated in the DRT of a temperature variation with a fixed gas mixture of $p_{H_2,FE} = 0.8$ atm and $p_{H_2O,FE} = 0.2$ atm in figure 4. The temperature covers a range of 600 °C to 900 °C. According to previous studies, the DRT can be divided into two major peaks in the low frequency $P_{LF,FE}$ and middle frequency range $P_{MF,FE}$ (6) as indicated in the DRT in figure 4. These contributions include gas diffusion, charge transfer reactions in the electrode and ionic transport in the CGO-matrix of the electrode. Obviously, all visible peaks in the DRT are thermally activated. Since a gas diffusion process should exhibit a $T^{0.5}$ temperature dependency, the direct correlation of one of those two DRT-peaks to the gas diffusion process is impossible (21). As gas diffusion is an unavoidable process in the fuel electrode, the observed temperature dependency of the DRT-peaks suggest that the gas diffusion process is covered by the thermally activated electrochemical processes (3, 13, 15, 16). Furthermore, three minor peaks are visible at frequencies above 100 Hz, which are not further analyzed in this study. Suggestions for their origin are given in (6).

Gas Transport Conditions. —The fuel gas supply of the symmetrical cell is shown in figure 5. Gas transport processes will occur in the gas channels of the flow field (convective and diffusive), the contact mesh (predominantly diffusive) and the porous fuel electrode (diffusive). This complex 3D setup is simplified to a virtual gas diffusion layer with a thickness L, whose impact on the gas diffusion resistance is modeled with the approach described in (29).

The dimensions of the gas channel, Ni contact mesh (34) as well as the porous fuel electrode are shown in table I. It becomes obvious that the thickness of the fuel electrode differs by more than one order of magnitude compared to the contact mesh and even more compared to the thickness of the gas channel. Since the gas diffusion resistance as discussed in (29) represents a function of the thickness of the gas diffusion layer L, which is dominated by the anode substrate in ASCs (20), the gas diffusion inside the just 24 µm thick porous fuel electrode in the investigated ESC presumably can be neglected (6), whereas gas diffusion in the Ni mesh and the gas channels has to be considered. With respect to "pore" diameters > 100 µm in gas channel and contact mesh, Knudsen diffusion can be neglected and the gas diffusion coefficients D_i are based on molecular gas diffusion solely. The Knudsen number Kn has been calculated for a temperature of 800 °C with a gas mixture of 0.5 atm H_2 and 0.5 atm H_2O and is shown in table I.

Therefore, the binary gas diffusion coefficients can be calculated by Chapman-Enskog (35, 36). Gas diffusion coefficients for components in a gas mixture with more than two components on total are calculated by Wilke (37).

According to Primdahl (29), the gas diffusion resistance $R_{diff,FE}$ at the fuel electrode can be calculated by equation [9].

$$R_{diff,FE} = \left(\frac{\tilde{R}T}{2F}\right)^2 \cdot \frac{L}{\Psi} \cdot \left(\frac{1}{D_{H_2} \cdot p_{H_2,FE}} + \frac{1}{D_{H_2O} \cdot p_{H_2O,FE}}\right) \cdot \frac{1}{P_{corr}} \qquad [9]$$

In this case, $\tilde{R}$ denotes the universal gas constant, T the temperature, Ψ the microstructure parameter within the gas diffusion layer, L the thickness of the gas diffusion layer, D_i the molecular gas diffusion coefficient of the component i, p_i the partial pressure of the component i and P_{corr} a conversion factor of 101330 Pa atm^{-1}.

In our setup the microstructure parameter Ψ and the thickness L represent unknown parameters, which can be summarized in an effective gas diffusion parameter G_{eff} accounting for an averaged diffusion length L in a (macroporous) medium with effective gas diffusion properties Ψ described by [10].

$$G_{\text{eff}} = \frac{\Psi}{L} \qquad\qquad [10]$$

This parameter, which is solely depending on geometrical and microstructural features of the test setup and the cell, is not depending on temperature or gas composition and thus can be used to calculate $R_{\text{diff,FE}}$ for arbitrary operating conditions.

Quantification of the Gas Diffusion Process. — In the following a procedure in order to overcome the overlap of activation and gas diffusion polarization in the spectrum with similar time constants is suggested. The subsequent experiment by the application of symmetrical cells with Ni/CGO fuel electrodes is designed to enlarge the gas diffusion resistance $R_{\text{diff,FE}}$ at the fuel electrodes (FE) with the help of equation [9] (29).

To analyze the gas diffusion process and quantify G_{eff}, a high accuracy test should be performed at operating conditions enlarging the gas diffusion resistance $R_{\text{diff,FE}}$. As $R_{\text{diff,FE}}$ is proportional to $T^{0.5}$, a high operating temperature of 850 °C is preferable, which also leads to a decrease of all thermally activated polarization processes. Also, low partial

pressures of the reactant $p_{\text{H}_2,\text{FE}} = 0.1$ atm and the reaction product $p_{\text{H}_2\text{O,FE}} = 0.05$ atm

with an appropriate balancing by inert gases, nitrogen and helium, are selected. This ensures reducing atmospheres to avoid Ni-oxidation and a sufficient content of steam to keep the charge transfer resistance at a low level. Based on the principles of the kinetic gas theory, we can apply two ternary gas mixtures with different gas diffusion properties as hydrogen and steam diffuse with different velocities in nitrogen or helium respectively. The molecular gas diffusion coefficients at 852 °C for hydrogen diffusing in the above-mentioned steam/nitrogen- and steam/helium-mixture differ by a factor of about 2:

$D_{\text{H}_2,(\text{H}_2\text{O,N}_2)} = 0.70 \cdot 10^{-3}$ m^2 s^{-1} and $D_{\text{H}_2,(\text{H}_2\text{O,He})} = 1.38 \cdot 10^{-3}$ m^2 s^{-1}.

The measured EIS spectra with corresponding DRT are shown in figure 6 for a symmetrical cell with Ni/CGO fuel electrodes. The application of two different inert gases results in a difference of the polarization resistance of 37 mΩcm^2 at a temperature of 852 °C. As the two inert gases are electrochemically inactive, other processes such as charge transfer and ionic charge transport are not affected and the difference in the spectra relies on gas diffusion solely, as shown by Sonn et al. (17) for the Ni/YSZ fuel electrode. This experiment proves the existence of a gas diffusion process, which is predominantly attributed to gas diffusion in the Ni mesh and the flow field. Observing the DRT of the symmetrical cell in figure 6 (b), the gas diffusion process becomes visible in a frequency range of

$0.4 - 100$ Hz and thus strongly overlaps with the charge transfer process in the fuel

electrode. It should be noted that the large gas diffusion contribution visible in the spectra are related to the selected operating conditions i.e. a highly diluted fuel.

The effective gas diffusion geometry parameter G_{eff} shall be obtained from the difference of the polarization resistances indicated in figure 6 (a). Based on the assumptions described above we claim that the difference of the polarization resistance between the gas mixture with nitrogen $R_{\text{pol,N}_2}$ and helium $R_{\text{pol,He}}$ equals the difference of the gas diffusion resistance in equation [11].

$$R_{\text{pol,N}_2} - R_{\text{pol,He}} \equiv R_{\text{diff,N}_2} - R_{\text{diff,He}} = \Delta R_{\text{diff}} \qquad [11]$$

We can now determine the unknown geometry parameter G_{eff} in equation [12].

$$G_{\text{eff}} = \left(\frac{\tilde{R}T}{2F}\right)^2 \cdot \frac{1}{\Delta R_{\text{diff}}} \cdot \frac{1}{P_{\text{corr}}} \cdot \ldots$$

$$\left[\frac{1}{D_{\text{H}_2,(\text{H}_2\text{O},\text{N}_2)} \cdot p_{\text{H}_2}} + \frac{1}{D_{\text{H}_2\text{O},(\text{H}_2,\text{N}_2)} \cdot p_{\text{H}_2\text{O}}} - \frac{1}{D_{\text{H}_2,(\text{H}_2\text{O},\text{He})} \cdot p_{\text{H}_2}} \right. \qquad [12]$$

$$\left. - \frac{1}{D_{\text{H}_2\text{O},(\text{H}_2,\text{He})} \cdot p_{\text{H}_2\text{O}}}\right]$$

With the help of the effective geometry parameter G_{eff} it is now possible to predict the gas diffusion resistance for any set of operating conditions using equation [9].

To evaluate reproducibility appropriate impedance measurements were conducted at different temperatures. The resulting differences in the polarization resistances $\Delta R_{\text{pol,FE}}$ of the symmetrical cells as well as the subsequent determined geometry parameters are listed in table II. Also, the mean value as well as the standard deviation at each temperature is shown. The calculation of the resulting effective gas diffusion geometry parameter G_{eff} is conducted with halved resistances to account for one electrode.

It should be noted that the observed deviations in G_{eff} are related to rather small variations of the measured polarization resistance (< 5 mΩcm²). Furthermore, the resulting $R_{\text{diff,FE}}$ is much smaller than the overall resistance of the cell and will become even smaller for realistic fuel mixtures without 85 % of inert gases. As discussed above, the accuracy in determining G_{eff} is increasing with increasing operating temperatures. Thus, the values at 902 °C with $G_{\text{eff}} = 736.87$ m⁻¹ are more reliable than those at much lower temperatures, where the activation polarization dominates the polarization resistance.

Determination of the Activation Polarization Resistance. — With the objective of establishing a dc cell model, polarization contributions in the impedance spectra of the electrodes can be simplified by RQ-elements (20) and more complex approaches as

transmission line models (23, 38) can be avoided. To quantify the activation polarization resistance $R_{act,FE}$ of the Ni/CGO fuel electrode, the low and middle frequency processes including the gas diffusion are summed up to obtain $R_{pol,FE}$. To account for one electrode the values from the CNLS-fit are divided by 2. Then the gas diffusion resistance $R_{diff,FE}$ is calculated according to equation [9] and subtracted in equation [13].

$$R_{act,FE} = R_{pol,FE} - R_{diff,FE} \qquad [13]$$

It is now possible to quantify the activation resistance of the Ni/CGO fuel electrode $R_{act,FE}$, which enables the further parameterization in order to develop a zero-dimensional cell model (21, 22). In comparison to a direct fitting of the spectra this approach provides a higher accuracy as G_{eff} is previously determined under ideal conditions enabling a precise calculation of $R_{diff,FE}$ for technically relevant operating points.

Activation Energy Fuel Electrode. —Figure 7 shows the resulting ASR values for activation processes of a single fuel electrode for a variation of temperature between 600 °C and 900 °C in steps of 50 °C with a gas mixture of $p_{H_2,FE} = 0.8$ atm and $p_{H_2O,FE} = 0.2$ atm according to the spectra in figure 4. The fuel electrode´s activation resistance indicates an Arrhenius behavior and therefore this approach is applied in order to determine the activation energy of the fuel electrode $E_{act,FE}$. The latter can be extracted by the slope of fitting equation [14] to the measured data.

$$R_{act,FE}(T) = B_{FE} \cdot \exp\left(\frac{E_{act,FE}}{\tilde{R}T}\right) \qquad [14]$$

This results in an activation energy of the fuel electrode of $E_{act,FE} = 90.54$ kJ mol^{-1} (0.94 eV) and a cell specific constant of $B_{FE} = 2.9517 \cdot 10^{-6}$ Ωcm^2.

Exponent a. — The determination of the exponent a in order to describe the hydrogen partial pressure dependency of the fuel electrode´s exchange current density follows the approach by Leonide et al. (21). Thus, the exponent a is extracted by a variation of the hydrogen partial pressure with a fixed amount of steam by adding nitrogen as an inert component to the fuel mixture. Therefore, a variation of the hydrogen partial pressure at 0.8 atm, 0.4 atm, 0.2 atm, 0.1 atm with a constant steam partial pressure of 0.2 atm and balanced with N₂, at $T = 754$ °C is shown in figure 8 (a) for a symmetrical cell. After determining the activation resistance $R_{act,FE}$ by subtracting the calculated gas diffusion resistance from the overlapping resistance it can now be plotted as a function of the hydrogen partial pressure in a double logarithmic scale in figure 8 (c). According to Leonide et al. (21), the exponent a can now be identified by the negative value of the slope in figure 8 (c) at 598 °C, 658 °C, 754 °C, 804 °C, 853 °C, and 902 °C.

Whereas in case of the Ni/YSZ fuel electrode the exponent a was not depending on temperature. In case of the Ni/CGO fuel electrode a significant temperature dependency of the exponent a is observed.

The resulting exponents are listed in table III. The differences are ranging over an order of magnitude with the accentuation of two temperature dependent plateaus ranging from approx. $600\ °C$ to $750\ °C$ and from $800\ °C$ to $900\ °C$ respectively.

Regarding low temperatures a mean value of $a(T = 600 - 750\ °C) = 0.035$ with a standard deviation of 0.013 and for higher temperatures a mean value of $a(T = 800 - 900\ °C) = 0.161$ with a standard deviation of 0.016 is found. The temperature dependency can be explained by the assumptions related to the application of a generalized Butler-Volmer (BV) approach in (21). The coupling of charge transfer and ionic transport in the active electrode volume is described by the overall activation resistance $R_{act,FE}$, which is subsequently used to calculate the parameters of the BV-equation. This approach was suitable for the Ni/YSZ-fuel electrode as the electrochemical reaction is limited to the three phase boundaries and the ionic conductivity of the YSZ-matrix is not affected by the oxygen partial pressure. Considering a Ni/CGO fuel electrode the situation is different. Ionic and electronic conductivity of CGO are depending on the oxygen partial pressure at the fuel electrode, i.e. the fuel gas composition and furthermore the electrochemical activity of the CGO-surfaces will be affected by gas composition and temperature. These complex interactions presumably result in the observed temperature dependency of the exponent a. The unexpected discontinuous temperature dependency cannot be further explained on the given data basis. A more comprehensive investigation of this observed temperature dependency has to be carried out.

Exponent b.— Subsequently, the exponent b in order to describe the steam partial pressure dependency of the fuel electrode´s exchange current density is determined by a variation of the steam partial pressure with a fixed amount of hydrogen and balanced with nitrogen (21). In figure 8 (b) DRTs of the symmetrical cell are shown for a variation of the steam partial pressure $p_{H_2O,FE}$ at $0.3\ atm$, $0.2\ atm$, $0.12\ atm$, $0.08\ atm$ and $0.04\ atm$ with a constant $p_{H_2,FE}$ of $0.6\ atm$ and balanced with N_2 at $T = 755\ °C$. The activation resistance $R_{act,FE}$ is determined by equation [13]. Similarly, impedance measurements under these conditions have been performed at $598\ °C$, $658\ °C$, $706\ °C$, $755\ °C$, $804\ °C$, $853\ °C$ and $902\ °C$. The results are plotted in figure 8 (d) and reveal a temperature dependency of the exponent b as well.

In addition, the resulting exponents are shown in figure 9 as a function of temperature and reveal a linear character.

This can be linearly fitted and described by equation [15].

$$b = \frac{0.0012}{\text{K}} \cdot T - 0.9892 \qquad [15]$$

Prefactor γ_{FE}. — The prefactor γ_{FE} can be described by equation [16] including the cell specific constant B_{FE} (21).

$$\gamma_{\text{FE}} = \frac{\tilde{R}T}{2FB_{\text{FE}}} \cdot \left[\left(\frac{p_{\text{H}_2,\text{FE}}}{p_{\text{ref}}}\right)^a \left(\frac{p_{\text{H}_2\text{O},\text{FE}}}{p_{\text{ref}}}\right)^b\right]^{-1} \qquad [16]$$

The above-mentioned evaluation for the cell specific constant B_{FE} has been operated for a fuel gas mixture of $p_{\text{H}_2,\text{FE}} = 0.8$ atm and $p_{\text{H}_2\text{O},\text{FE}} = 0.2$ atm by varying temperature with an overall pressure $p = 1$ atm. Therefore, these conditions are applied in order to determine the prefactor γ_{FE} (21). In addition, a temperature dependency of the exponents a and b has been identified as shown above, which has to be included when calculating γ_{FE} in equation [17].

$$\gamma_{\text{FE}}(T) = 1.46 \cdot 10^5 (\text{A m}^{-2}\text{K}^{-1}) \cdot \left[(0.8)^{a(T)} \cdot (0.2)^{b(T)}\right]^{-1} \cdot T \qquad [17]$$

The fuel electrode is now fully parametrized except for the charge transfer coefficient.

Charge Transfer Coefficient. — In contrast to the previously discussed parameters obtained from symmetrical cells at OCV, the charge transfer coefficient α_{EL} has to be determined from full cells in a polarized state. Considering a cell exhibiting a Ni/YSZ fuel electrode, different charge transfer coefficients have been found for SOEC and SOFC mode (21,22). This shall be examined for the full cell with a Ni/CGO fuel electrode as well.

In this contribution, the charge transfer coefficient of the LSCF air electrode α_{AE} could not be characterized adequately, because the polarization resistance of the air electrode is smaller compared to the fuel electrode and being overlapped by the latter in the spectrum. Therefore, the charge transfer coefficient of the air electrode is assumed to be equal to the one determined by Leonide et al. (21) as it is the same type of electrode and thus $\alpha_{\text{AE}} = 0.65$ is assumed.

Regarding the SOEC mode -0.1 A cm^{-2}, -0.2 A cm^{-2}, -0.4 A cm^{-2} as well as -0.6 A cm^{-2} with a fuel gas mixture of $p_{\text{H}_2,\text{FE}} = 0.38$ atm (balance H$_2$O) with synthetic air at the air electrode at $T = 745$ °C was set, which is shown in the DRT in figure 10 (a). Further, for SOFC mode a fuel gas mixture of $p_{\text{H}_2,\text{FE}} = 0.8$ atm (balance H$_2$O) with pure oxygen at the air electrode at $T = 750$ °C by varying the load starting from 0.05 A cm^{-2} up to 0.25 A cm^{-2} in steps of 0.05 A cm^{-2} was applied. Pure oxygen is used in order to minimize processes at the air electrode. The corresponding results are appearing in figure 10 (b). Also, measurement artifacts have been omitted at frequencies larger than 10^4 Hz.

In the following, the two main contributions in the lower and middle frequency range are summarized to R_{load} and is plotted for the two modes in figure 11 (a) and (b) respectively. It can be described by a second-degree polynomial fit as a function of the current density j in equation [18].

$$R_{\mathrm{load}}(j) = \frac{\partial \eta_{\mathrm{load}}}{\partial j} = q_1 \cdot j^2 + q_2 \cdot j \cdot + q_3 \qquad [18]$$

The corresponding coefficients q_1, q_2 and q_3 are listed in table IV.

The integration of equation [18] leads to an overpotential in equation [19]. In order to obtain the activation overpotential at the fuel electrode, the overpotential for gas diffusion at the fuel electrode and activation at the air electrode is calculated and subtracted at the corresponding current density. In this case, the gas diffusion at the air electrode is neglected. Under OCV-conditions ($j = 0$) results $\eta_{\mathrm{act,FE}}(j = 0) = 0$ and therefore, q_4 levels zero.

$$\eta_{\mathrm{act,FE}}(j) = \frac{1}{3} \cdot q_1 \cdot j^3 + \frac{1}{2} \cdot q_2 \cdot j^2 + q_3 \cdot j + q_4 - \eta_{\mathrm{diff,FE}}(j) \qquad [19]$$
$$- \eta_{\mathrm{act,AE}}(j)$$

With the help of equation [19] the activation overpotential can now be calculated as a function of the current density j and is plotted in figure 11 (c) and (d) for SOEC and SOFC mode respectively. These curves can be described with the Butler-Volmer equation and with the help of the Matlab$^{\mathrm{tm}}$-solver fsolve the charge transfer coefficients can be extracted.

Regarding the SOEC mode a charge transfer coefficient of $\alpha_{\mathrm{FE,SOEC}} = 0.59$ and for SOFC mode $\alpha_{\mathrm{FE,SOFC}} = 0.76$ results.

Ohmic Losses. — In order to quantify the ohmic losses the thermal behavior of the area specific ohmic resistance $R_{\mathrm{ohm}}(T)$ is investigated for a full cell. For this purpose, a fuel gas mixture of 0.8 atm H_2 (balance H_2O) as well as synthetic air at the air electrode was set at temperatures of 600 °C, 651 °C, 700 °C, 750 °C, 800 °C, 850 °C, and 897 °C. The validation of the zero-dimensional model has been examined with this full cell as well. Thus, the logarithm of temperature divided by the area specific ohmic resistance is plotted in figure 12 corresponding to the logarithm of the ionic conductivity times temperature as a function of temperature. By assuming a temperature independent activation energy of the ohmic losses it can be determined by the slope of the linear fit with the help of the Arrhenius equation for the area specific ohmic resistance [3]. As can be seen in figure 12, this cannot be sufficiently applied, because a slight deviation can be seen at temperatures higher than 800 °C and subsequently two sections of temperature are visible in order to describe the Arrhenius behavior. A non-linear description is therefore necessary in order to quantify the ohmic losses.

Thus, considering that the ohmic losses are dominating in an electrolyte-supported compared to a fuel electrode-supported cell and combined with less doping of the 3YSZ compared to 8YSZ, the temperature dependency of the ohmic activation energy cannot be neglected. Therefore, the ohmic resistance shall be described by a parabola-fit. At first, equation [3] is transferred dimensionless in equation [20] by Ωcm^2 in order to take the logarithm of it. Subsequently, it shall be equaled with $y = k_1 x^2 + k_2 x + k_3$ in equation [21], where the variable x denotes $x = \frac{1000K}{T}$ with K denoting the unit Kelvin.

$$y = \ln\left(\frac{R_{ohm}(T)}{\Omega cm^2}\right) = \ln\left(\frac{T}{B_{ohm}} \cdot \frac{1}{\Omega cm^2}\right) + \frac{E_{act,ohm}}{\tilde{R}T} \qquad [20]$$

$$\ln\left(\frac{1000K}{B_{ohm}} \cdot \frac{1}{\Omega cm^2} \cdot \frac{1}{x}\right) + \frac{E_{act,ohm}}{1000K \cdot \tilde{R}} \cdot x = k_1 x^2 + k_2 x + k_3 \qquad [21]$$

We assume that the original approach by extracting the ohmic activation energy $E_{act,ohm}$ from the linear slope can be transferred to the parabola likewise in order to extract the ohmic activation energy from the slope of the parabola. Therefore, equation [21] is derived by x and solved for $E_{act,ohm}$ in equation [22]. The latter can now be described as a function of temperature.

$$E_{act,ohm} = 1000K \cdot \tilde{R}\left(2k_1 x + k_2 + \frac{1}{x}\right) \qquad [22]$$

Subsequently, the cell specific parameter B_{ohm} can be obtained by solving equation [21] to equation [23].

$$B_{ohm} = \frac{1000K}{x}\frac{1}{\Omega cm^2} \cdot \exp\left(-\left(k_1 x^2 + k_2 x + k_3 - \frac{E_{act,ohm}}{1000K \cdot \tilde{R}} \cdot x\right)\right) \qquad [23]$$

Finally, the parabola fit is shown in figure 13 with a sufficient agreement to the ohmic resistance.

By applying the introduced method, the polynomial coefficients can be obtained and are listed in table V.

Model Parameters. — The relevant parameters in order to model the current-voltage behavior in a zero-dimensional approach are listed in table VI. Apart from the adaptions described above, no further changes in the model and its parameterization (21) were necessary. Furthermore, the parameters have been varied independently in order to investigate their sensitivity towards the model. The experimentally obtained voltage at a current density of 0.5 A cm^{-2} with a gas mixture of 0.65 atm H$_2$ (balanced with H$_2$O) at a

temperature 850 °C was chosen as a reference. Therefore, the last column in table VI indicates the deviation from the simulated in relation to the measured voltage, when the parameter is varied by ± 20 % in its value and thus showing the sensitivity towards the model.

It becomes obvious, that the model is mostly sensitive towards the cell specific constant regarding the ohmic losses B_{ohm}. The ohmic losses in this particular case with the empirical determination presented above are independent of the ohmic activation energy. Another parameter with high impact represents the activation energy of the fuel electrode $E_{act,FE}$. All other parameters only show a rather small influence when varied by ± 20 %.

Model Validation. — The cell voltage can now be modeled with equation [1] and further equations given in (21) as all of the unknown parameters are determined. The model covers operating temperatures from 600 °C to 900 °C with arbitrary fuel mixtures of hydrogen and steam in a cell voltage range from 600 to 1400 mV. To obtain an excellent agreement with measured CV-characteristics the temperature increase due to self-heating of the cell has to be considered in the model. This was realized by using the cell temperature measured by a thermocouple approx. 2 mm above the cell surface. Furthermore, the measured open circuit voltage is used in order to correct minor leakages below 2 % in the test bench. Exemplary, a validation is shown for a fuel gas mixture of 0.65 atm H_2 in figure 14 (a) and 0.35 atm H_2 in (b) (balanced with H_2O) and synthetic air at the air electrode.

The developed zero-dimensional cell model represents the measured current-voltage behavior in excellent agreement with a deviation ≤ 3 % for both SOFC and SOEC mode. The remaining deviation between calculated and measured current-voltage curves is most probably caused by the difference between the internal cell temperature (electrolyte temperature) and the measured temperature (39).

It is now possible to quantify the individual loss contributions (figure 15). Regarding the investigated ESC the ohmic losses are dominating the cell performance as expected. An about one order of magnitude smaller overvoltage has to be attributed to the activation losses at the fuel electrode. The fuel and air electrodes gas diffusion losses as well as the air electrode activation losses (testing with synthetic air) are in the range of a few mV only and thus can almost be neglected. Gas diffusion losses in the cathode can only be analyzed at very low oxygen partial pressures in the applied setup. It should be noticed that this can change drastically if the cell is contacted by a thin contact layer in a stack (40).

Conclusions
In this contribution, we presented a zero-dimensional dc model of an electrolyte-supported cell with a Ni/CGO fuel electrode. The experimental parameterization via electrochemical impedance spectroscopy enables the model to precisely predict current-voltage characteristics over wide temperature and gas composition ranges. In order to carry out an unambiguous

process identification and subsequent quantification of the loss contributions, the Ni/CGO fuel electrode required a methodology for isolating and quantifying the gas diffusion process at the fuel electrode. This was implemented by altering the inert gas component in a ternary fuel gas mixture. The difference in polarization resistances between two different inert gas components, namely nitrogen and helium, can be used to determine an effective gas diffusion geometry parameter, which enables the calculation of the gas diffusion resistance for arbitrary operating conditions. Using this procedure, the loss contributions of gas diffusion and activation within a Ni/CGO fuel electrode have been successfully separated and quantified for the first time. The excellent capability of the model for accurate cell performance prediction has been shown by the comparison of measured and calculated CV-curves over a wide range of operating conditions in both SOFC and SOEC mode.

Appendix

The characterization of the air electrode follows the approach by Leonide et al. (21) with no further extension regarding the extraction of the model parameters. In addition, no further significant results were observed during this work. That´s why, this part is shown in the appendix with the determination of the microstructure parameter Ψ_{AE}, the activation energy $E_{act,AE}$, the exponent m and the prefactor γ_{AE} of the air electrode.

Equivalent Circuit Model Air Electrode. — Processes occurring at the LSCF air electrode are described with the equivalent circuit model developed by Leonide et al. (21), which has been used in previous studies (33, 41). Though, gas diffusion is described by an RQ-element. Furthermore, the coupling of charge transfer and solid-state diffusion of oxygen ions is specified by a Gerischer-element (42). As mentioned above, processes at higher frequencies are accounted for the ohmic resistance.

Microstructure Parameter Air Electrode. — In this work an LSCF air electrode likewise to Leonide et al. (21) is applied. The loss mechanisms at the air electrode become isolated by observing symmetrical cells. Figure A-1 (a) shows the DRT of a variation of the oxygen partial pressure of a symmetrical cell with LSCF electrodes with a gas mixture of 0.05 atm, 0.02 atm and 0.01 atm oxygen (balanced with N_2) at a temperature of 800 °C. The gas diffusion process becomes visible in a frequency range of $0.5 - 10$ Hz (21) and it´s contribution to the polarization resistance is extracted with a CNLS-fit. The resulting gas

diffusion resistance using the ASR values of a single electrode are shown in a double logarithmic plot in figure A-1 (b).

In addition, the gas diffusion resistance shall be derived starting from equation [8] with transferring it to equation [A-1] by the logarithmic law with the microstructure parameter Ψ_{AE}, the gas diffusion length L_{AE}, the gas diffusion coefficient for oxygen D_{O_2}.

$$\eta_{\text{diff,AE}} = -\frac{\tilde{R}T}{4F}\ln\left(1 - \frac{\tilde{R}TL_{AE}\left(1 - \frac{p_{O_2,AE}}{p}\right)}{4F\Psi_{AE}D_{O_2}p_{O_2,AE}P_{corr}} \cdot j\right) \qquad [A-1]$$

The derivation of equation [A-1] and at open-circuit leads to equation [A-2] with the gas diffusion resistance at the air electrode $R_{\text{diff,AE}}$.

$$R_{\text{diff,AE}} = \left.\frac{\partial\eta_{\text{diff,AE}}}{\partial j}\right|_{j=0} = \left(\frac{\tilde{R}T}{4F}\right)^2 \cdot \frac{L_{AE}}{\Psi_{AE}} \cdot \frac{1}{D_{O_2}}\left(\frac{1}{p_{O_2,AE}} - \frac{1}{p}\right) \cdot \frac{1}{P_{corr}} \qquad [A-2]$$

The trend of the gas diffusion resistance as a function of the oxygen partial pressure can now be approximated with the help of equation [A-2] using a solver with a least-squares method in order to determine the unknown microstructure parameter Ψ_{AE} of the air electrode.

Thereby, the gas diffusion length in this case remains unknown. Though, the gas diffusion within the gold-mesh is contributing to it as well (34). For the purpose of comparison to the work of Leonide (21), the gas diffusion length is set to the thickness of the single air electrode of 47 µm from the symmetrical cell. Also, Knudsen-Diffusion needs to be considered in this case as well (21). Therefore, the gas diffusion coefficient for oxygen is calculated by the Bosanquet-approach with the help of the molecular gas diffusion coefficient $(D_{O_2,mol} = 1.7879 \cdot 10^{-4}\ \text{m}^2\ \text{s}^{-1},\ T = 800\ °C)$ as well as Knudsen-Diffusion coefficient D_{Kn,O_2}. An estimated pore radius of 600 nm was set for the determination of D_{Kn,O_2} resulting to $D_{Kn,O_2} = 3.3705 \cdot 10^{-4}\ \text{m}^2\ \text{s}^{-1}$ at a temperature of 800 °C.

Finally, a microstructure parameter of $\Psi_{AE} = 0.048$ is resulting. In this case, the trend of the measured gas diffusion resistance cannot be described precisely enough with equation [A-2]. The latter can presumably be explained by the application of a revised generation of LSCF electrodes with a likely higher porosity. Imprecision also might be explained by an estimated pore diameter. The application of a pore size distribution could not have been performed in the frame of this work.

Activation Energy Air Electrode. —In order to determine the activation energy of the air electrode $E_{\text{act,AE}}$ a variation of temperature between 600 °C and 900 °C in steps of 50 °C with a gas mixture of $p_{O_2} = 0.21$ atm (balanced with N_2) of a symmetrical air electrode is shown in figure A-2. At comparably low frequencies between $10 - 20$ Hz the gas diffusion process becomes visible, as it only shows a slight correlation with temperature. In a frequency range between $100 - 400$ Hz the activation process of the air electrode indicates a clear activation by temperature. In the equivalent circuit model, this process is described by a Gerischer element (33). By extracting the activation resistance with a CNLS-fit, it can be plotted in an Arrhenius-plot in figure A-3 using the ASR values of a single air electrode. Here, a grey area is marked with resistances of less than 10 mΩcm², indicating the possibility of measurement imprecisions as the boundaries of the frequency response analyzer are reached. But, this does not seem to have an influence yet.

The linear trend leads to Arrhenius behavior resulting in an activation energy of the air electrode of $E_{\text{act,AE}} = 144.54$ kJ mol⁻¹ from the value of the slope. In addition, the cell specific constant yields to $B_{\text{AE}} = 1.5185 \cdot 10^{-10}$ Ωcm². In comparison, the LSCF electrode characterized by Leonide (21) holds values of $E_{\text{act,AE}} = 139.86$ kJ mol⁻¹ and

$B_{\text{AE}} = 4.032 \cdot 10^{-9}$ Ωcm². The deviation between the activation energies is less than 3 % and with regard to a state-of-the-art electrode comparably small. Further, the cell specific constant in this case is smaller, which presumably can be explained by the application of synthetic air with 0.21 atm O_2 and 0.79 atm N_2. Thereby, contaminants (43) as they are present in air from the environment can be neglected.

In addition, the activation resistances of the fuel electrode (using the ASR values of a single electrode) are displayed as well and differ by an order of magnitude to the air electrode. Therefore, the activation process of the latter presumably can be neglected when simulating the dc mode as shown above.

Exponent m. — The extraction of the exponent m describing the oxygen partial pressure dependency of the air electrode´s exchange current density follows the approach by Leonide et al. (21) as well. In figure A-4 (a) the DRT of a symmetrical cell with LSCF air electrodes is shown at a temperature of $T = 800$ °C. The data is based on a variation of the oxygen partial pressure with 0.21 atm, 0.12 atm, 0.05 atm, 0.02 atm, 0.01 atm (balanced with N_2). Subsequently, in figure A-4 (b) the resulting activation resistance using the ASR values of a single air electrode is plotted in a double logarithmic scale as a function of the oxygen partial pressure and fitted with a power law approach. The exponent m is then extracted by the negative value of the slope of the fit resulting to a value of $m = 0.42$. In comparison to Leonide et al., the exponent m in this case is about a factor of two larger.

Prefactor γ_{AE}. — The exponential prefactor γ_{AE} can be determined with the help of equation [A-3] (21). The above-mentioned evaluation of the variation of temperature was

performed with $p_{O_2} = 0.21$ atm with an overall pressure of $p = 1$ atm. Thus, these conditions were set in order to determine the prefactor γ_{AE}. With the above-mentioned exponent m and the cell specific constant B_{AE} a value of

$\gamma_{AE}(T) = 5.47 \cdot 10^9 \; (\mathrm{A \; m^{-2} \; K^{-1}}) \cdot T$ results in contrast with

$\gamma_{AE}(T) = 1.52 \cdot 10^8 (\mathrm{A \; m^{-2} K^{-1}}) \cdot T$ from Leonide (21).

$$\gamma_{AE} = \frac{\tilde{R}T}{2FB_{AE}} \cdot \left[\left(\frac{p_{O_2}}{p_{ref}} \right)^m \right]^{-1} \qquad \text{[A-3]}$$

Nomenclature

latin letters

a	exponent describing hydrogen partial pressure dependency of the fuel electrode´s exchange current density (-)
b	exponent describing steam partial pressure dependency of the fuel electrode´s exchange current density (-)
B_{ohm}	cell specific constant for ohmic resistance (K Ω^{-1} m^{-2})
B_{EL}	cell specific constant for electrodes (Ωm^2)
D_i	gas diffusion coefficient of the component i (m^2 s^{-1})
D_{ijk}	ternary gas diffusion coefficient with the components i, j and k (m^2 s^{-1})
$D_{\mathrm{Kn},i}$	Knudsen-Diffusion coefficient (m^2 s^{-1})
E_{act}	activation energy (J mol^{-1})
F	Faraday constant (As mol^{-1})
G_{eff}	effective gas diffusion parameter (m^{-1})
j	current density (A m^{-2})
$j_{0,El}$	exchange current density (A m^{-2})
k_1, k_2, k_3	polynomial coefficients
m	exponent describing oxygen partial pressure dependency of the fuel electrode´s exchange current density (-)
p	overall pressure (atm)
p_{ref}	reference pressure $=$ 1 atm
p_i	partial pressure of the component i
P_{corr}	conversion factor 101330 (Pa atm^{-1})
$P_{\mathrm{LF,FE}}$	low frequency process at fuel electrode (-)
$P_{\mathrm{MF,FE}}$	middle frequency process at fuel electrode (-)
q_1, q_2, q_3, q_4	polynomial coefficients
$\tilde{R}$	universal gas constant 8.314 (J mol^{-1} K^{-1})
R_{diff}	gas diffusion resistance (Ωm^2)
R_{pol}	polarization resistance (Ωm^2)
R_{act}	activation resistance (Ωm^2)
ΔR_{diff}	difference of the gas diffusion resistance (Ωm^2)
ΔR_{pol}	difference of the polarization resistance (Ωm^2)
R_{ohm}	ohmic resistance (Ωm^2)
T	temperature (K)
U_{OCV}	open circuit voltage (V)
U_{cell}	cell voltage (V)
x	variable
y	variable
z	number of exchanged electrons (-)

greek letters

α	charge transfer coefficient (-)
γ	exponential prefactor (A m^{-2})
δ	concentration of oxygen lattice vacancy (-)
ε	porosity (-)
η	overpotential (V)
σ	standard deviation
Ψ	microstructure parameter (-)

subscripts

act	activation
AE	air electrode
cell	cell
corr	correction
diff	gas diffusion
eff	effective
EL	electrode
FE	fuel electrode
H_2	hydrogen
H_2O	steam
He	helium
Kn	Knudsen
LF	low frequency
load	electrical load
MF	middle frequency
N_2	nitrogen
OCV	open-circuit voltage
ohm	ohmic
pol	polarization
por	pore

abbreviations

Al_2O_3	aluminum oxide
ASC	anode-supported cell
ASR	area specific resistance
AE	air electrode
BV	Butler-Volmer
CGO	Gadolinium-Doped Ceria
CNLS	complex non-linear least square
CV	current-voltage

dc	direct current	
DRT	distribution of relaxation times	
EIS	electrochemical impedance spectroscopy	
EL	electrode	
ESC	electrolyte-supported cell	
FE	fuel electrode	
FIB	focused ion beam	
He	helium	
H_2	hydrogen	
H_2O	steam	
lin	linear	
LSCF	$La_{0.6}Sr_{0.4}Co_{0.2}Fe_{0.8}O_{3-\delta}$	
MSC	metal-supported cell	
N_2	nitrogen	
O_2	oxygen	
OCV	open-circuit-voltage	
RQ	parallel connection of ohmic resistance and constant-phase element	
SOC	solid oxide cell	
SOEC	solid oxide electrolyzer cell	
SOFC	solid oxide fuel cell	
sym-an1	symmetrical cell with Ni/CGO fuel electrodes 1	
sym-an2	symmetrical cell with Ni/CGO fuel electrodes 2	
3D	three-dimensional	
3YSZ	3 mol-% yttria-stabilized zirconia	
8YSZ	8 mol-% yttria-stabilized zirconia	

References

1. D. Udomsilp, C. Lenser, O. Guillon, and N. H. Menzler, *Energy Technol.*, 2001062 (2021).

2. J. Mermelstein, M. Millan, and N. Brandon, *J. Power Sources*, **195** (6), 1657, (2010).

3. V. A. Rojek-Wöckner, A. K. Opitz, M. Brandner, J. Mathé, and M. Bram, *J. Power Sources*, **328**, 65 (2016).

4. M. Riegraf, M. P. Hoerlein, R. Costa, G. Schiller, and K. A. Friedrich, *ACS Catal.*, **7**, 7760 (2017).

5. F. Thaler, D. Udomsilp, W. Schafbauer, C. Bischof, Y. Fukuyama, Y. Miura, M. Kawabuchi, S. Taniguchi, S. Takemiya, A. Nenning, A. K. Opitz, M. Bram, *J. Power Sources*, **434**, 226751 (2019).

6. M. Riegraf, R. Costa, G. Schiller, K. A. Friedrich, S. Dierickx, and A. Weber, *J. Electrochem. Soc.*, **166** (13), F865 (2019).

7. T. Nakamura, T. Kobayashi, K. Yashiro, A. Kaimai, T. Otake, K. Sato, J. Mizusaki, and T. Kawada, *J. Electrochem. Soc.*, **155** (6), B563 (2008).

8. K. Eguchi, T. Setoguchi, T. Inoue, and H. Arai, *Solid State Ionics*, **52**, 165-172 (1992).

9. J. W. Fergus, *Solid State Ionics*, **177**, 1529-1541 (2006).

10. S. Primdahl and M. Mogensen, *Solid State Ionics*, **152-153**, 597-608 (2002).

11. M. Mogensen, S. Primdahl, M. J. Jørgensen, and C. Bagger, *J. Electroceramics*, **5**, 141-152 (2000).

12. A. Weber, T. Dickel, and E. Ivers-Tiffée, *EFCF Proceedings*, 48 (2016).

13. A. Weber, S. Dierickx, N. Russner, and E. Ivers-Tiffée, *ECS Trans.*, **77** (10), 141 (2017).

14. A. Nenning, M. Holzmann, J. Fleig, A.K. Opitz, *Mater. Adv.*, **2**, 5422-5431 (2021).

15. M. Riegraf, V. Yurkiv, R. Costa, G. Schiller, and K. A. Friedrich, *ChemSusChem*, **10** (3), 587 (2017).

16. A. Nenning, C. Bischof, J. Fleig, M. Bram, and A. K. Opitz, *Energies*, **13** (4), 987 (2020).

17. V. Sonn, A. Leonide, and E. Ivers-Tiffée, *J. Electrochem. Soc.*, **155** (7), B675 (2008).

18. P. V. Aravind, J. P. Ouweltjes, and J. Schoonman, *J. Electrochem. Soc.*, **156** (12), B1417 (2009).

19. A. M. Houssain, J. V.T. Høgh, T. Jacobsen, and N. Bonanos, *Int. J. Hydrog. Energy*, **37** (5), 4309 (2012).

20. A. Leonide, V. Sonn, A. Weber, and E. Ivers-Tiffée, *J. Electrochem. Soc.*, **155** (1), B36 (2008).

21. A. Leonide, Y. Apel and E. Ivers-Tiffée, *ECS Trans.*, **19** (20), 81-109 (2009).

22. J.-C. Njodzefon, D. Klotz, A. Kromp, A. Weber, and E. Ivers-Tiffée, *J. Electrochem. Soc.*, **160** (4), F313 (2013).

23. S. Dierickx, T. Mundloch, A. Weber, and E. Ivers-Tiffée, *J. Power Sources*, **415**, 69 (2019).

24. H. Schichlein, A. C. Müller, M. Voigts, A. Krügel, and E. Ivers-Tiffée, *J. Appl. Electrochem.*, **32**, 875 (2002).

25. A. Kromp, J. Nielsen, P. Blennow, T. Klemensø, and A. Weber, *Fuel Cells*, **13** (4), 598-604 (2013).

26. Th. Franco, R. Mücke, A. Weber, M. Haydn, M. Rüttinger, N. H. Menzler, A. Venskutonis, L. S. Sigl and, H.-P. Buchkremer, *EFCF Proceedings*, A0906 (2012).

27. D. Klotz, A. Weber, and E. Ivers-Tiffée, *Electrochim. Acta,* **227**, 110-126 (2017).

28. S. B. Beale, M. Andersson, C. Boigues-Muñoz, H. L. Frandsen, Z. Lin, S. J. McPhail, M. Ni, B. Sundén, A. Weber and, A. Z. Weber, *Prog. Energy Combust. Sci.*, **85**, 100902 (2021).

29. S. Primdahl and M. Mogensen, *J. Electrochem. Soc.*, **146** (8), F2827 (1999).

30. J. Kim, A. V. Virkar, K. Fung, K. Mehta, and S. C. Singhal, *J. Electrochem. Soc.*, **146** (1), 69-78 (1999).

31. M. Meffert, F. Wankmüller, H. Störmer, A. Weber, P. Lupetin, E. Ivers-Tiffée, and D. Gerthsen, *Fuel Cells*, **20** (5), 580-591 (2020).

32. M. Schönleber, D. Klotz and E. Ivers-Tiffée, *Electrochim. Acta*, **131**, 20-27 (2014).

33. C. Endler-Schuck, A. Leonide, A. Weber, S. Uhlenbruck, F. Tietz, and E. Ivers-Tiffée, *J. Power Sources*, **196** (17), 7257 (2011).

34. H. Geisler, *Finite Element Method (FEM) Model and Performance Analysis of Solid Oxide Fuel Cells*, KIT Scientific Publishing, Karlsruhe (2019).

35. E. L. Cussler, Diffusion: Mass Transfer in Fluid Systems, Cambridge University

Press, (1995).

36. B. E. Poling, J. M. Prausnitz, and J. P. O`Connell, *The properties of gases and liquids*, 5. Ed. McGraw-Hill (2007).

37. D. F. Fairbanks and C. R. Wilke, *Ind. Eng. Chem.*, **42** (3), 471-475, (1950).

38. A. Weber, *TM Technisches Messen*, **88** (1), 1-16 (2021).

39. D. Klotz, J.-C. Njodzefon, A. Weber, and E. Ivers-Tiffée, *ECS Trans.*, **45** (1), 523-530 (2012).

40. H. Geisler, M. Kornely, A. Weber, and E. Ivers-Tiffée, *ECS Trans.*, **57** (1), 2871-2881 (2013).

41. A. Kromp, A. Leonide, A. Weber, and E. Ivers-Tiffée, *J. Electrochem. Soc.*, **158** (8), B980-B986 (2011).

42. S. B. Adler, J. A. Lane, and B. C. H. Steele, *J. Electrochem. Soc.*, **143** (11), 3554 (1996).

43. F. G. Kerry, *Industrial gas Handbook: gas Separation and Purification*, CRC Press, (2007).

Tables

TABLE I. Dimensions and microstructural parameters of gas channel, Ni contact mesh (34) and porous fuel electrode as well as Knudsen criteria Kn. ([c]SEM, [d]estimated)

	thickness	width, pore diameter	porosity ε_{por}	Kn
	µm	µm	-	-
gas channel	1000	1000	1	$4.4 \cdot 10^{-4}$
Ni contact mesh (34)	≈ 240	≈ 250	≈ 0.64	$18 \cdot 10^{-4}$
porous fuel electrode	$\approx 24^{(c)}$	$< 0.6^{(d)}$	$\approx 0.35^{(d)}$	0.73

TABLE II. Difference of the polarization resistances $\Delta R_{pol,FE}$ of the symmetrical cells with Ni/CGO fuel electrodes for sym-an1 and sym-an2 for a gas mixture of 0.1 atm H_2, 0.05 atm H_2O, balanced with N_2 and He respectively. The calculation of the resulting effective gas diffusion geometry parameter G_{eff} is conducted with halved resistances to account for one electrode.

sym-an1			sym-an2			mean value	standard deviation
T	$\Delta R_{pol,FE}$	G_{eff}	T	$\Delta R_{pol,FE}$	G_{eff}	$\bar{G}_{eff}$	σ
°C	mΩcm^2	m^{-1}	°C	mΩcm^2	m^{-1}	m^{-1}	m^{-1}
753	43	627.66	755	42	642.93	635.30	7.63
803	38	719.32	804	41	666.85	693.09	26.24
852	37	747.75	853	40	691.84	719.80	27.96
902	38	736.87	902	38	736.87	736.87	0

TABLE III. Temperature dependency of the exponent a between $600\ ^\circ C$ and $900\ ^\circ C$.

temperature °C	a -
598	0.019
658	0.035
754	0.051
804	0.166
853	0.139
902	0.178

Table IV. Coefficients of the second-degree polynomial describing R_{load} as a function of the current density j.

Operating-mode	q_1	q_2	q_3
SOEC	0.0294	0.0344	0.1212
SOFC	-0.1057	0.0015	0.1138

Table V. Polynomial coefficients for an active area of $1\ cm^2$ in order to describe the ohmic resistance in the Arrhenius plot in figure 13.

experimental full cell	k_1	k_2	k_3
	3.8374	1.9162	-5.5970

TABLE VI. Model parameters of the zero-dimensional cell model (21) adapted to a solid oxide cell with Ni/CGO fuel electrode, 3YSZ electrolyte and LSCF air electrode.

Parameter	Unit	Value	Sensitivity $+20\%, -20\%$
$E_{act,ohm}$	J mol^{-1}	$1000\text{K} \cdot \tilde{R}\left(2k_1 x + k_2 + \frac{1}{x}\right)$ with $x = \frac{1000\text{K}}{T}$	-
B_{ohm}	K $(\Omega\text{m}^2)^{-1}$	$\frac{1000\text{K}}{x}\frac{10^4}{\Omega\text{m}^2} \cdot \exp\left(-\left(k_1 x^2 + k_2 x + k_3 - \frac{E_{act,ohm}}{1000\text{K} \cdot \tilde{R}} \cdot x\right)\right)$	$+4.4\%, -8\%$
k_1	-	3.8374	-
k_2	-	1.9162	-
k_3	-	-5.5970	-
$E_{act,FE}$	kJ mol^{-1}	90.54	$-9.3\%, +1.6\%$
B_{FE}	Ωm^2	$2.95 \cdot 10^{-10}$	$-1\%, 0\%$
$a(T = 600 - 750\ °\text{C})$	-	0.035	-
$a(T = 800 - 900\ °\text{C})$	-	0.161	$-0.6\%, -0.6\%$
$b(T)$	-	$\frac{0.0012}{\text{K}} \cdot T - 0.9892$	$-0.5\%, -0.7\%$
$\gamma_{FE}(T)$	A m^{-2}	$1.46 \cdot 10^5 (\text{A m}^{-2}\text{K}^{-1}) \cdot \left[0.8^{a(T)} \cdot 0.2^{b(T)}\right]^{-1} \cdot T$	-
$\alpha_{FE,SOEC}$	-	0.59	-
$\alpha_{FE,SOFC}$	-	0.76	$-0.4\%, -0.7\%$
G_{eff}	m^{-1}	736.87	$-0.5\%, -0.6\%$
$E_{act,AE}$	kJ mol^{-1}	144.54	$-1.7\%, -0.5\%$
B_{AE}	Ωm^2	$1.5185 \cdot 10^{-14}$	$-0.6\%, -0.6\%$
m	-	0.42	$-0.6\%, -0.6\%$
$\gamma_{AE}(T)$	A m^{-2}	$5.47 \cdot 10^9 (\text{A m}^{-2}\text{K}^{-1}) \cdot T$	-
α_{AE}	-	0.65 (21)	$-0.6\%, -0.6\%$
Ψ_{AE}	-	0.048	$-0.6\%, -0.6\%$

Figures

- ▦ LSCF AE (1 cm x 1 cm; ≈ 30 μm)

- ▦ LSCF potential probes (≈ 30 μm)
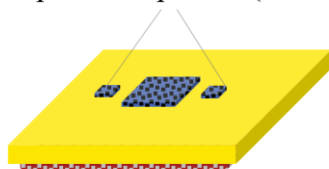
- ■ 3YSZ electrolyte (5 cm x 5 cm; ≈ 85 μm)

- ▦ Ni/CGO FE (4 cm x 4 cm; ≈ 24 μm)

Figure 1. Schematic sketch of experimental full cell with a Ni/CGO fuel electrode, 3YSZ electrolyte, LSCF air electrode as well as LSCF potential probes for OCV monitoring.
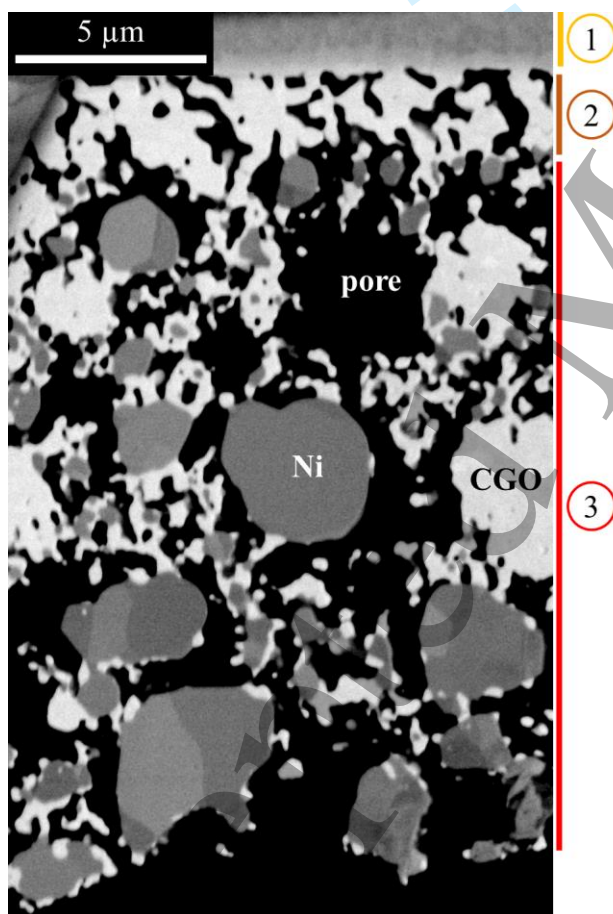
Figure 2. SEM image of a FIB-polished fuel electrode cross-section with a 3YSZ electrolyte in cell layer 1, a CGO interlayer 2 and a Ni/CGO fuel electrode 3 with Ni particles (darker grey), CGO particles (lighter grey) and black pores in between; mirror detector, electron energy: 5 keV, electron beam current: 0.4 nA.
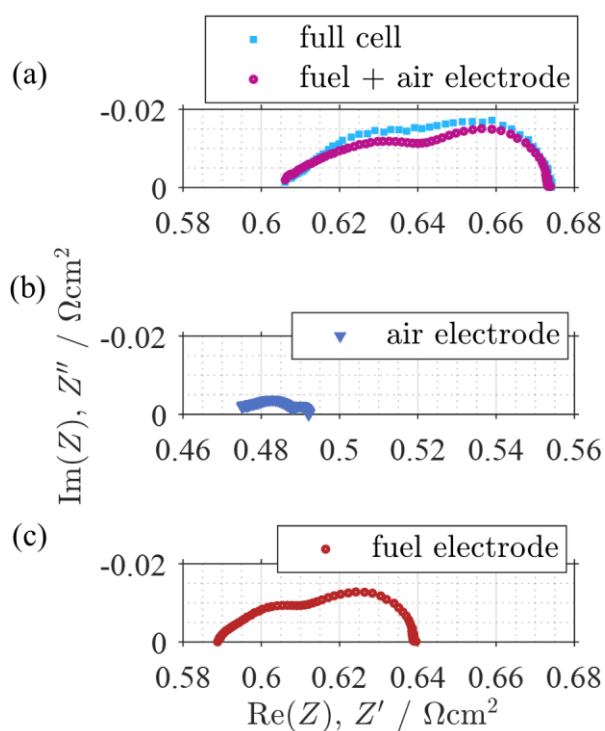
Figure 3.   (a) spectra of full cell and sum of fuel and air electrode ($T =$ 800 °C, fuel gas mixture of 0.65 atm H_2 (balanced with H_2O) and synthetic air at the air electrode), (b) the LSCF air electrode ($T =$ 800 °C, synthetic air as oxidant) and (c) a Ni/CGO fuel electrode ($T =$ 806 °C, fuel gas mixture of 0.65 atm H_2 (balanced with H_2O)).
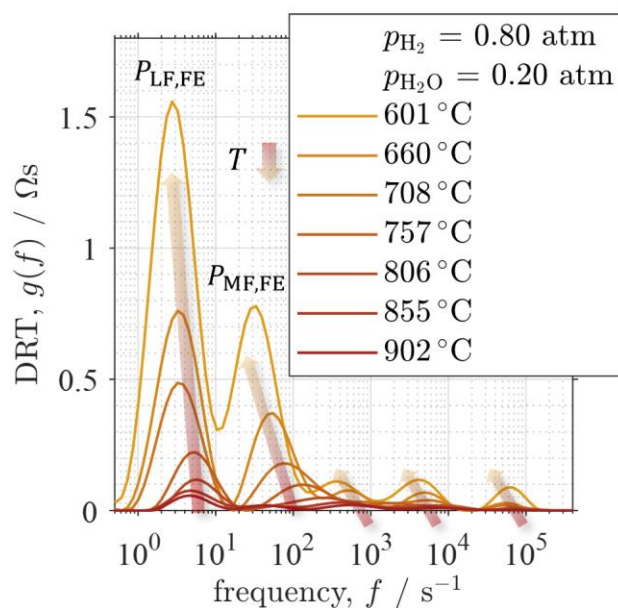
Figure 4.   DRTs of spectra measured during a temperature variation between 600 °C and 900 °C with a gas mixture of $p_{H_2,FE} = 0.8$ atm and $p_{H_2O,FE} = 0.2$ atm of a symmetrical cell with Ni/CGO fuel electrodes.
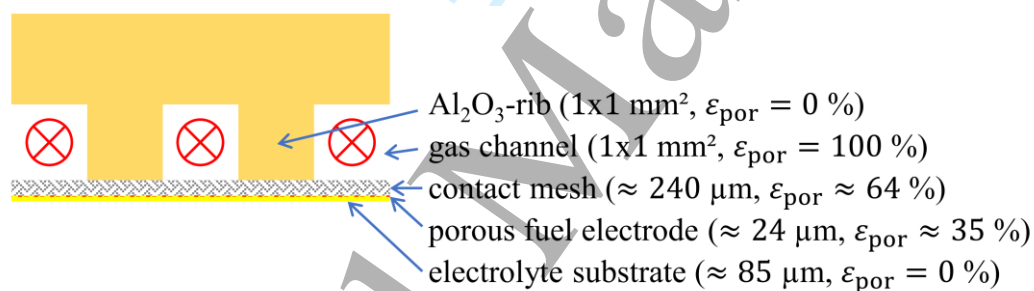
Figure 5.   Sketch of the gas transport along the cell´s surface in the cell test setup. In the 1 cm² test benches a stack like gas supply via gas channels is employed. Details can be found in (27).
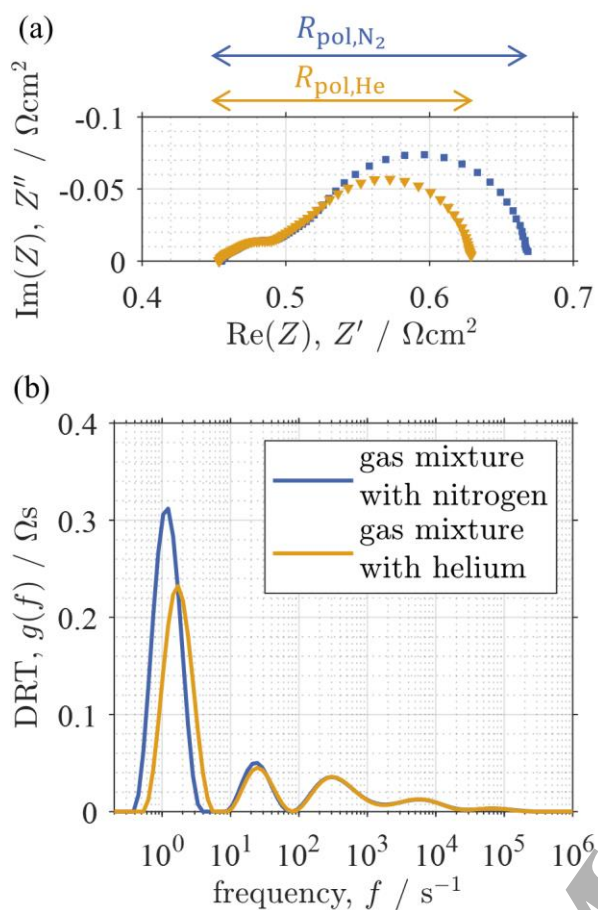
Figure 6. (a) Impedance spectra and (b) DRT of a symmetrical cell with Ni/CGO fuel electrodes with two ternary gas mixtures with the inert gases nitrogen and helium respectively ($T = 852°C$, gas composition: 0.1 atm H_2, 0.05 atm H_2O, 0.85 atm inert gas).
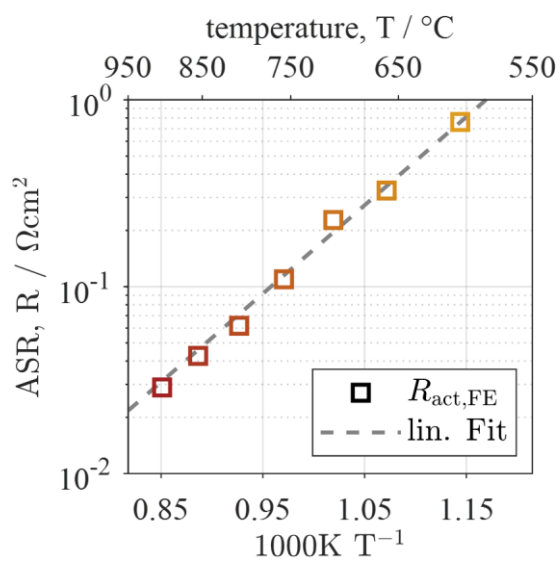
Figure 7. Arrhenius-Plot of a temperature variation between $600\,°C$ and $900\,°C$ in steps of $50\,°C$ with a gas mixture of $p_{H_2,FE} = 0.8$ atm and $p_{H_2O,FE} = 0.2$ atm, using the ASR values of a single fuel electrode.
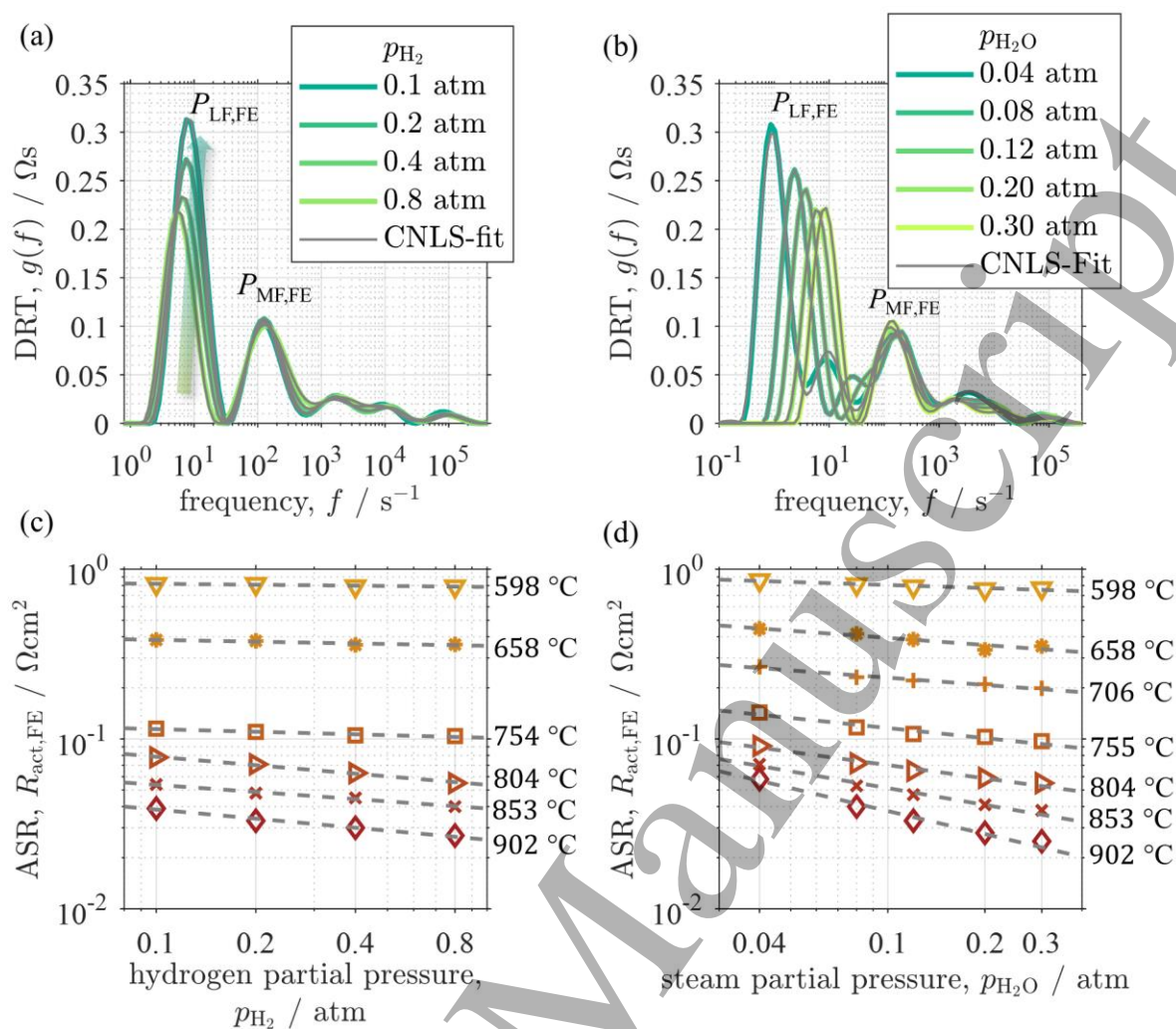
Figure 8. DRTs of a symmetrical cell with Ni/CGO fuel electrodes for a variation of (a) the hydrogen partial pressure $p_{H_2,FE}$ at 0.8 atm, 0.4 atm, 0.2 atm, 0.1 atm with a constant steam partial pressure $p_{H_2O,FE}$ of 0.2 atm and balanced with N$_2$, at $T = 754$ °C and (b) with a variation of the steam partial pressure $p_{H_2O,FE}$ at 0.3 atm, 0.2 atm, 0.12 atm, 0.08 atm and 0.04 atm with a constant $p_{H_2,FE}$ of 0.6 atm and balanced with N$_2$, at $T = 755$ °C. (c) Determination of the exponent a, and (d) of the exponent b, at temperatures between 600 °C and 900 °C in steps of approx. 50 °C using the ASR-values of a single electrode.
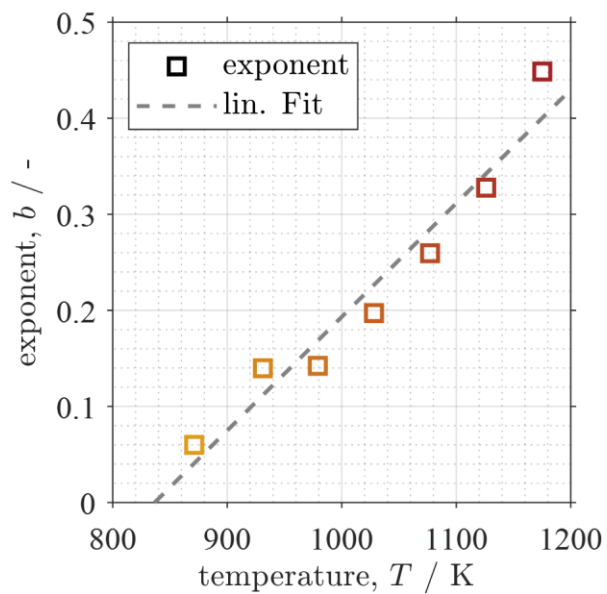
Figure 9. Temperature dependency of the exponent b with a linear fit ($R^2 = 0.9435$).
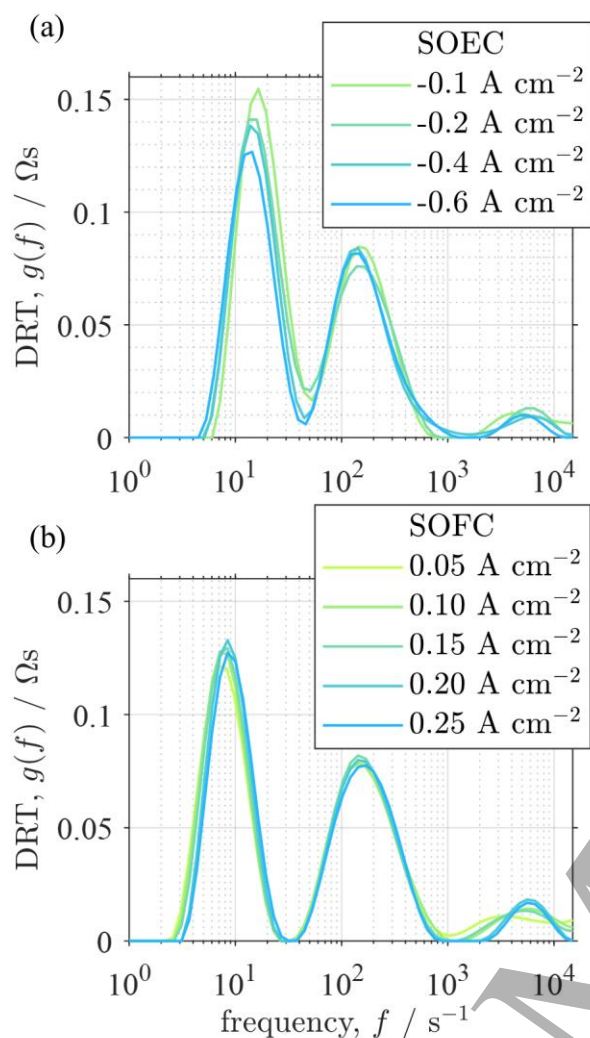
Figure 10.   (a) DRT of the variation of the electrical load in SOEC mode with a fuel gas mixture of $p_{H_2,FE} = 0.38$ atm (balance H$_2$O) with synthetic air at the air electrode at $T = 745$ °C and (b) DRT of a variation of the electrical load in SOFC mode with a fuel gas mixture of $p_{H_2,FE} = 0.8$ atm (balance H$_2$O) with pure oxygen at the air electrode at $T = 750$ °C.
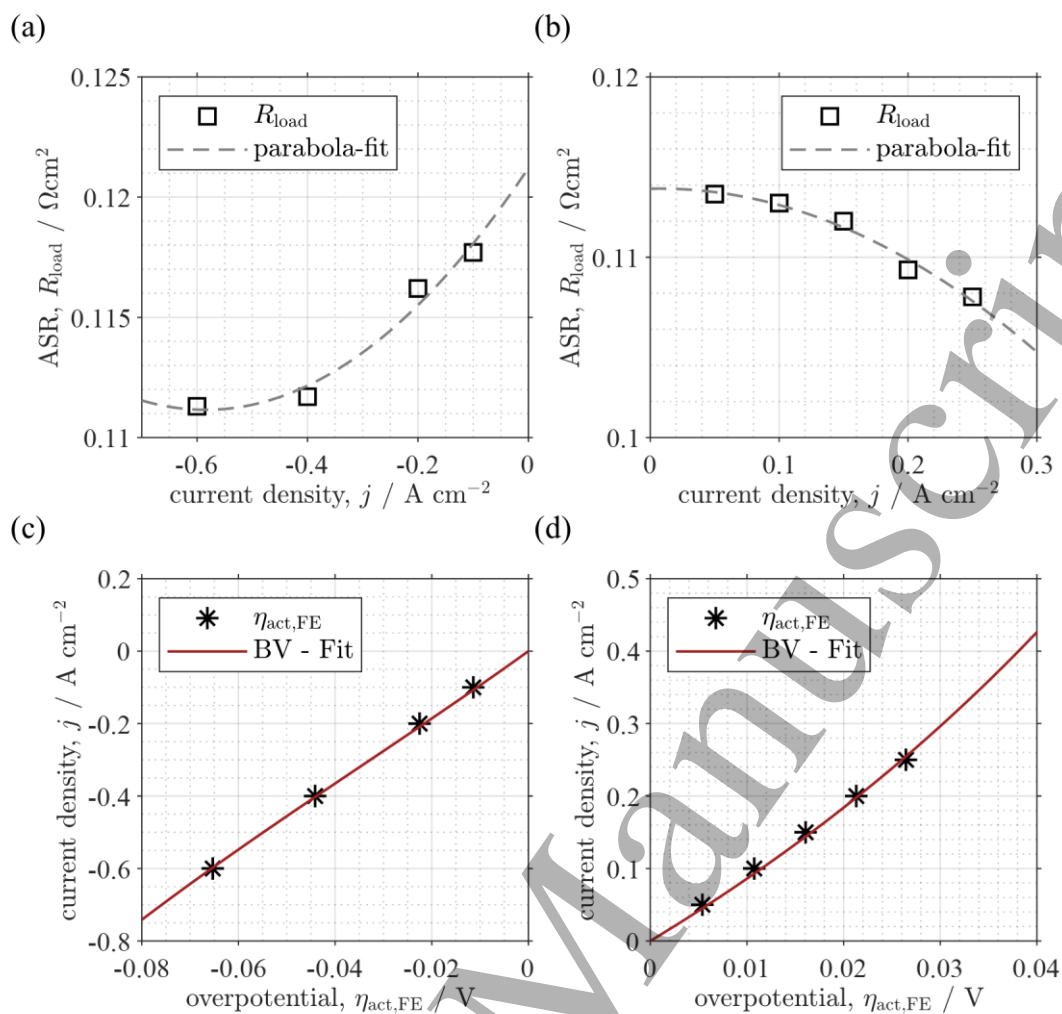
Figure 11.   (a) Resistance $R_{\mathrm{load}}(j)$ as a function of the current density in SOEC mode with a fuel gas mixture of $p_{\mathrm{H_2,FE}} = 0.38$ atm (balance H₂O) with synthetic air at the air electrode at $T = 745$ °C. (c) Determination of the charge transfer coefficient in SOEC mode. (b) Resistance $R_{\mathrm{load}}(j)$ as a function of the current density in SOFC mode with a fuel gas mixture of $p_{\mathrm{H_2,FE}} = 0.8$ atm (balance H₂O) with pure oxygen at the air electrode at $T = 750$ °C. (d) Determination of the charge transfer coefficient in SOFC mode.
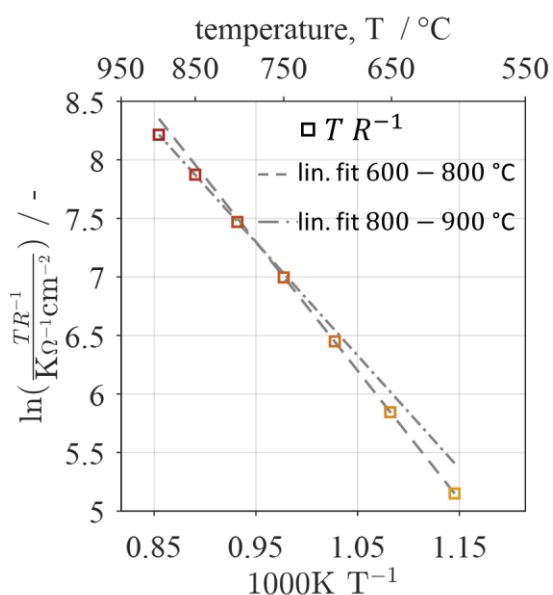
Figure 12. Plot of the temperature divided by the area specific ohmic resistance R_{ohm} of a full cell as a function of temperature with separate linear fits in two sections of temperature with (i) $600 - 800$ °C and (ii) $800 - 900$ °C with a fuel gas mixture of 0.8 atm H_2 (balance H_2O) as well as synthetic air at the air electrode.
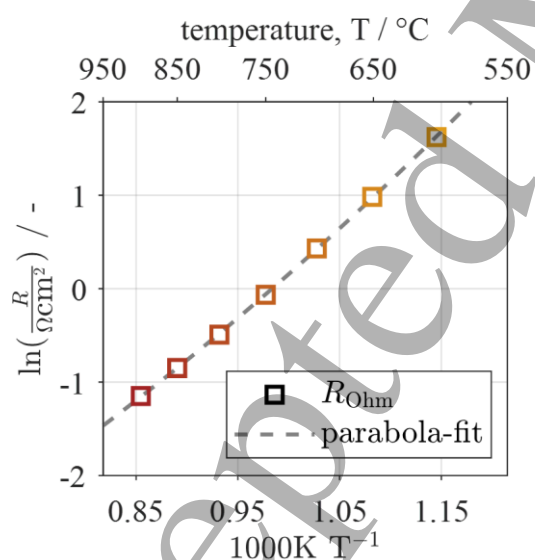
Figure 13. Arrhenius-plot of the area specific ohmic resistance R_{ohm} for a temperature variation of 600 °C, 651 °C, 700 °C, 750 °C, 800 °C, 850 °C, and 897 °C with a second-degree polynomial fit for a fuel gas mixture of 0.8 atm H_2 (balance H_2O) and synthetic air at the air electrode.
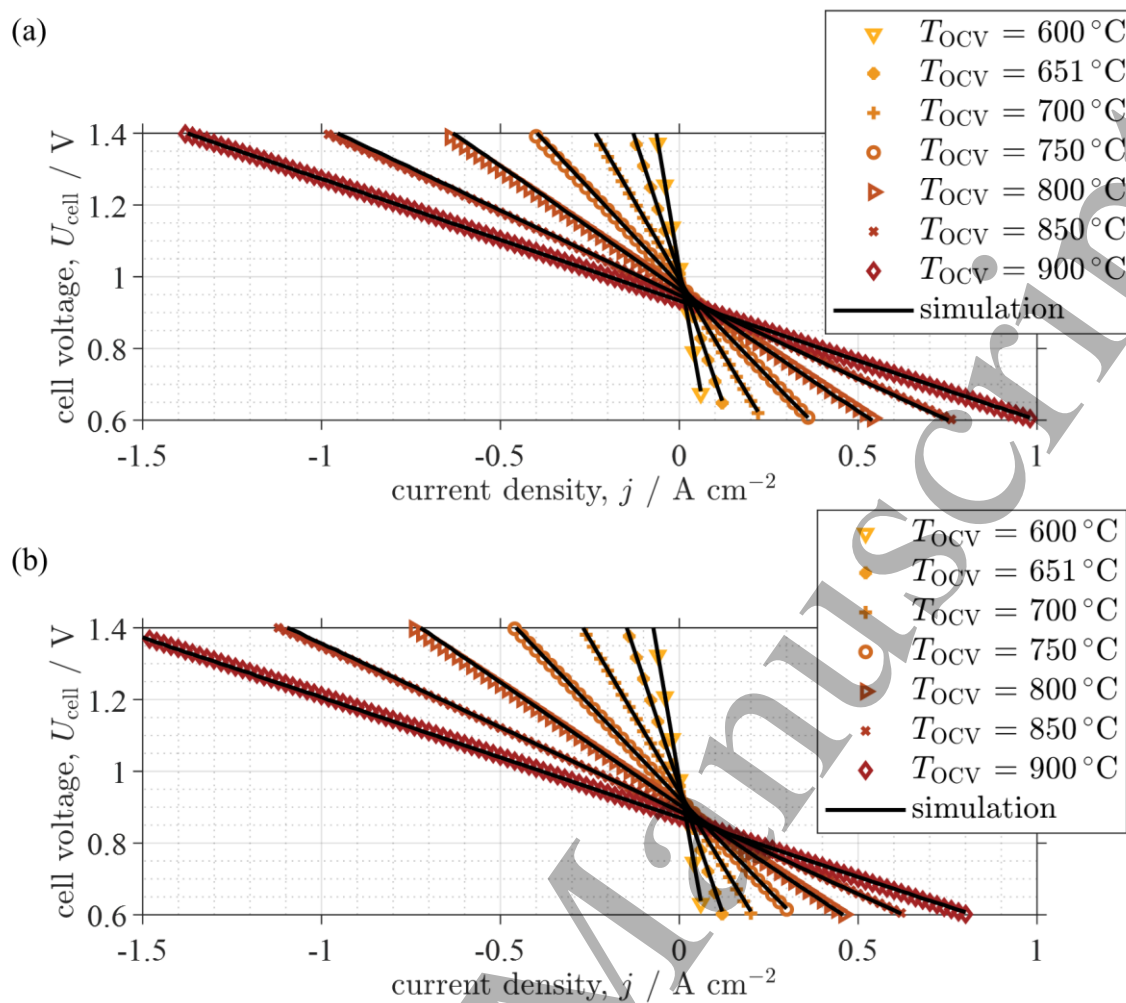
Figure 14. Variation of temperature between 600 °C and 900 °C with measured as well as simulated (continuous line) current-voltage characteristics for SOEC and SOFC mode with a fuel gas mixture of 0.65 atm H_2 (a) and of 0.35 atm H_2 (b) balanced with H_2O and synthetic air as the oxidant.
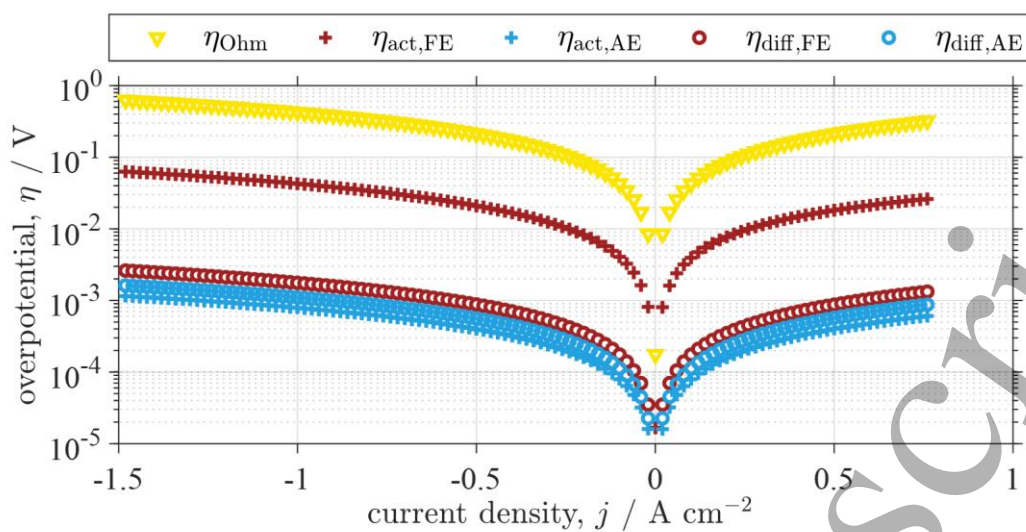
Figure 15. Absolute values of the ohmic η_{ohm}, activation $\eta_{\mathrm{act,FE/AE}}$ as well as gas

diffusion losses $\eta_{\mathrm{diff,FE/AE}}$ as a function of the current density j in SOEC and SOFC mode

with a fuel gas mixture of 0.65 atm H_2 (balanced with H_2O) and synthetic air at the air
electrode with $T_{\mathrm{OCV}} = 850\ °C$.
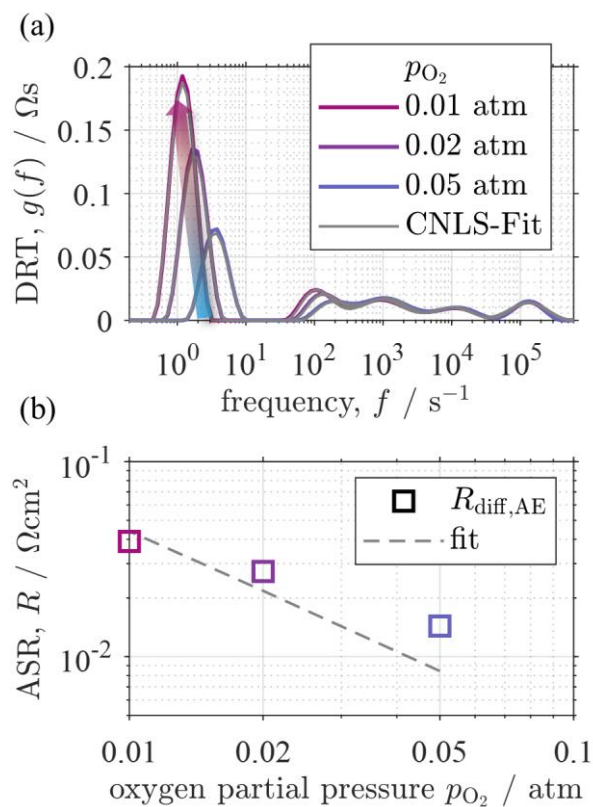
Figure A-1. (a) DRT of a variation of the oxygen partial pressure of a symmetrical cell with LSCF electrodes with a gas mixture of 0.05 atm, 0.02 atm and 0.01 atm oxygen (balanced with N_2) at a temperature of 800 °C and (b) gas diffusion resistance from CNLS-fit using ASR values of a single electrode.
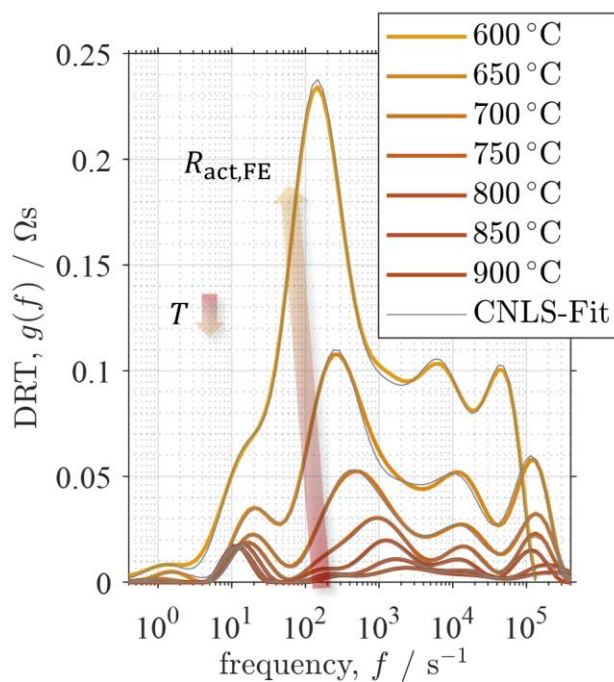
Figure A-2. DRT of a temperature variation between 600 °C and 900 °C in steps of 50 °C with a gas mixture of $p_{O_2} = 0.21$ atm (balanced with N_2) of a symmetrical air electrode.
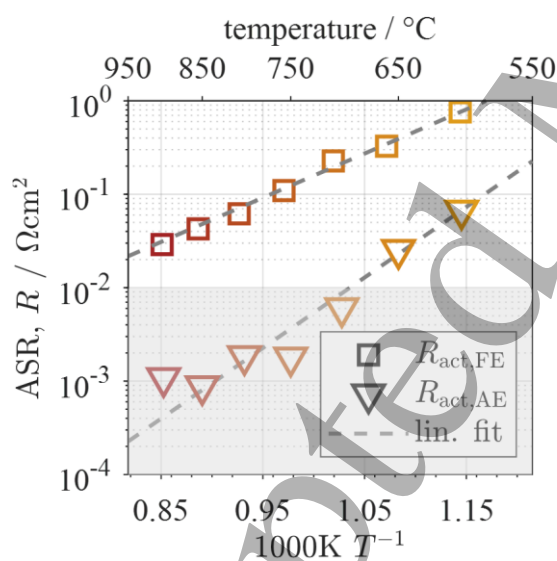
Figure A-3. Arrhenius plot for a temperature variation from 600 °C to 900 °C in steps of 50 °C using the ASR values of a single fuel electrode with a gas mixture of 0.8 atm H_2 (balance H_2O) and a single air electrode with 0.21 atm O_2.
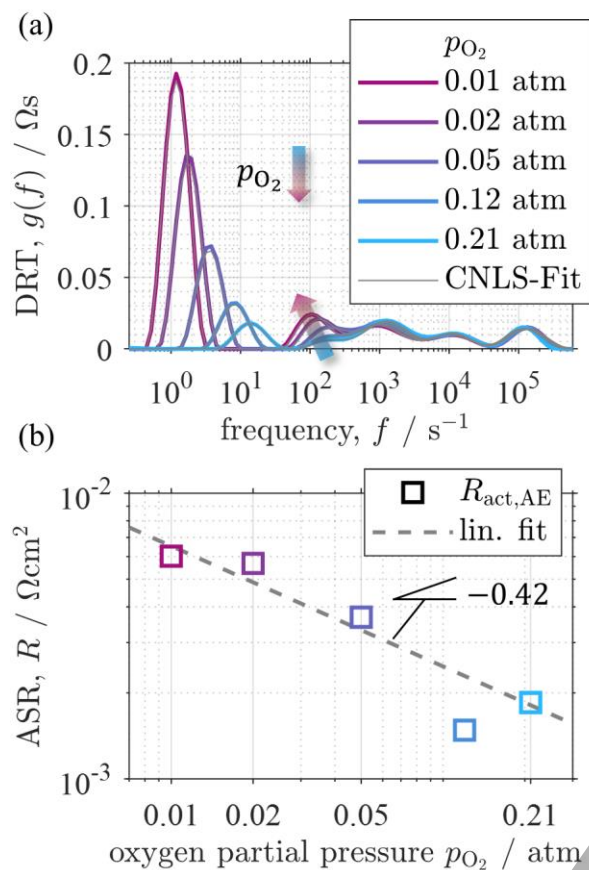
Figure A-4. (a) DRT of a variation of the oxygen partial pressure at a temperature of $T = 800$ °C with 0.21 atm, 0.12 atm, 0.05 atm, 0.02 atm, 0.01 atm (balanced with N₂) and (b) determination of the exponent m using the ASR values of a single electrode.